

# Hierarchical MoS<sub>2</sub>/Ni<sub>3</sub>S<sub>2</sub> core-shell nanofibers for highly efficient and stable overall-water-splitting in alkaline media

Faze Wang<sup>a, b</sup>, Hao Wu<sup>a</sup>, Hong Sun<sup>a</sup>, Li Ma<sup>d</sup>, Wenzhong Shen<sup>a</sup>, Yanbo Li<sup>b, \*</sup>,  
Maojun Zheng<sup>a, c, \*\*</sup>

<sup>a</sup> Key Laboratory of Artificial Structure and Quantum Control, Ministry of Education, Department of Physics and Astronomy, Shanghai Jiao Tong University, Shanghai, 200240, China

<sup>b</sup> Institute of Fundamental and Frontier Sciences, University of Electronic Science and Technology of China, Chengdu, 610054, China

<sup>c</sup> Collaborative Innovation Center of Advanced Microstructures, Nanjing University, Nanjing, 210093, China

<sup>d</sup> School of Chemistry and Chemical Technology, Shanghai Jiao Tong University, Shanghai, 200240, China

## ARTICLE INFO

### Article history:

Received 14 July 2018

Received in revised form

26 August 2018

Accepted 11 September 2018

### Keywords:

Molybdenum disulfide

Ammonium intercalation

Earth abundant catalyst

Hydrogen evolution reaction

Overall water splitting

## ABSTRACT

Non-noble metal electrocatalysts replacing Pt catalyst for efficient hydrogen-evolution reaction (HER) are highly desired to achieve sustainable production of H<sub>2</sub> through water splitting. In this paper, we report a novel ammonium intercalated MoS<sub>2</sub>/Ni<sub>3</sub>S<sub>2</sub> core-shell nanofibers on graphene-Ni foam by a facile method. Such hierarchical nanostructures provide abundant active sites for hydrogen evolution. Furthermore, DFT calculation demonstrates that the intercalated ammonium ions improve the chemisorption of protons for MoS<sub>2</sub>, thus further enhancing HER activity. The synthesized MoS<sub>2</sub>/Ni<sub>3</sub>S<sub>2</sub> nanofiber cathode exhibits an overpotential of 109 mV at 10 mA cm<sup>-2</sup> in 1 M KOH electrolyte – the lowest overpotential reported so far among any earth-abundant cathodes working in strong alkaline condition. Combining with a nickel iron layered double hydroxide anode, stable overall water splitting with a low potential of 1.59 V at 10 mA cm<sup>-2</sup> is achieved in 1 M KOH for 100 h.

© 2018 Elsevier Ltd. All rights reserved.

## 1. Introduction

The increasing energy demand caused by burning fossil fuels and the global energy crises have led to the intense search for alternative fuel, hydrogen, as an ideal energy carrier in chemical form, has been actively pursued as a promising renewable energy to substitute the traditional fossil fuels [1–3]. Electrocatalytic water splitting is considered to be a simple and effective pathway for hydrogen production [4–10]. Among the proposed configurations for overall water splitting, the dual functional electrochemical cell constructed by electrically connecting an anode and a cathode in series is the most economical one that has the potential to realize excellent performance required for practical application. Constructing such an electrocatalytic cell requires the anode and cathode with high

activity to work in the same electrolyte to simplify the system. Although many highly active and stable hydrogen evolution reaction (HER) cathodes working in acidic condition have been developed in recent years, only a few precious metal catalysts (i.e., RuO<sub>x</sub> and IrO<sub>x</sub>) can evolve oxygen efficiently in acidic media. Constructing overall water splitting cells working in acidic media using these catalysts is not economical. As most of the earth abundant oxygen evolution reaction (OER) catalysts developed so far exhibit high activity in alkaline medium, it is highly desirable that earth-abundant HER cathode having high activity and stability in alkaline media is developed to combine with earth-abundant OER anodes for efficient and stable overall water splitting.

Two-dimensional (2D) layered material, particularly molybdenum disulfide (MoS<sub>2</sub>) has been explored extensively as HER electrocatalysts [11–17]. Both theoretical and experimental studies demonstrated that the HER activity sites located along the Mo-S edges of the 2D MoS<sub>2</sub> layer [18–21]. Hence, much attention has been devoted to preparing nanostructured MoS<sub>2</sub> with a high proportion of exposed edges [22–27] and lower intrinsic resistance [27–31] using physical and chemical strategies to boost HER catalytic performance. Besides the morphological nanostructure

\* Corresponding author. Institute of Fundamental and Frontier Sciences, University of Electronic Science and Technology of China, Chengdu, 610054, China.

\*\* Corresponding author. Key Laboratory of Artificial Structure and Quantum Control, Ministry of Education, Department of Physics and Astronomy, Shanghai Jiao Tong University, Shanghai, 200240, China.

E-mail addresses: [yanboli@uestc.edu.cn](mailto:yanboli@uestc.edu.cn) (Y. Li), [mjzheng@sjtu.edu.cn](mailto:mjzheng@sjtu.edu.cn) (M. Zheng).

engineering of MoS<sub>2</sub>, much effort has been devoted to octahedral metallic (1T) phase MoS<sub>2</sub> which exhibited superior HER catalytic activity to those with trigonal prismatic (2H) phase due to enhanced intrinsic catalytic activity facilitating the charge transfer and the chemisorption of protons. Through the intercalation of Li<sup>+</sup> ions, new active sites can be created on the basal planes of 1T phase MoS<sub>2</sub> [32–35]. However, 1T-LiMoS<sub>2</sub> was not stable in the media and its fabrication process is relatively complicated [36–39]. Therefore, facile fabrication of stable 1T-MoS<sub>2</sub> is highly desirable. So far, the electrochemical HER by chemically exfoliated 1T MoS<sub>2</sub> materials has been studied well in acidic solution, while the catalytic HER in alkaline solution and rationally designed nanostructures of 1T MoS<sub>2</sub> are still rarely studied.

Herein, we report a facile synthesis of a hierarchical ammonium intercalated A-MoS<sub>2</sub>/Ni<sub>3</sub>S<sub>2</sub> core-shell nanostructures on graphene-Ni foam. Metallic phase MoS<sub>2</sub> shell and Ni<sub>3</sub>S<sub>2</sub> nanofiber core were grown in a single hydrothermal step on graphene-Ni foam. The wrinkled MoS<sub>2</sub> shells provide a large effective surface area for catalytic reaction, while the in-situ grown Ni<sub>3</sub>S<sub>2</sub> nanofibers cores allow efficient charge transfer to the Ni foam substrate. More importantly, such MoS<sub>2</sub>/Ni<sub>3</sub>S<sub>2</sub> core-shell heterostructures exhibit a highly efficient HER activity in 1 M KOH. DFT calculation reveals that the existence of ammonium between the MoS<sub>2</sub> (002) planes facilitate the chemisorption of protons, leading to the improvement for electrochemical hydrogen generation. The combined effects of nanostructure and ammonium intercalation make such A-MoS<sub>2</sub>/Ni<sub>3</sub>S<sub>2</sub>/graphene/Ni foam cathode catalyst exhibit a low overpotential of 109 mV at 10 mA cm<sup>-2</sup> in 1 M KOH electrolyte. The high HER activity in strong alkaline condition makes it possible to combine with a state-of-the-art oxygen evolution anode that performs well in alkaline media for efficient overall water splitting. Indeed, when combined with a nickel iron layered double hydroxide (NiFe-LDH) anode, stable overall water splitting with a low potential of 1.59 V at 10 mA cm<sup>-2</sup> was demonstrated in 1 M KOH for 100 h.

## 2. Results and discussion

Graphene was firstly deposited on the nickel foam as a soft template for the growth of Ni<sub>3</sub>S<sub>2</sub> nanostructures [40]. Graphene wrapped nickel foam was obtained by an interfacial redox reaction. Since the reduction potential of graphene oxide is much higher than that of nickel, GO nanosheets can be reduced and spontaneously grow on the surface of Ni surfaces. Fig. S1 shows the scanning electron microscopy (SEM) images of nickel foam and as-obtained GN. It can be seen from high magnification SEM image that a thin layer of graphene film with some ripples and wrinkles is uniformly grown on NF surface. The surface of Ni foam remains its integrity after high temperature treatment.

The typical Raman spectrum recorded from the GN clearly demonstrate the two characteristics carbon bonding bands, i.e., the D-band around 1346 cm<sup>-1</sup> related to disordered sp<sup>2</sup> carbon and the G-band around 1590 cm<sup>-1</sup> related to well-ordered graphite (Fig. S2). After hydrothermal treatment, the intensity ratio of D to G peaks (*I<sub>D</sub>*/*I<sub>G</sub>*) increases from 0.77 to 1.02. The change in the *I<sub>D</sub>*/*I<sub>G</sub>* ratio indicates a decrease in the average size of the re-established G network (sp<sup>2</sup> carbon), confirming the reduction of GO.

The A-MoS<sub>2</sub>/Ni<sub>3</sub>S<sub>2</sub> core-shell nanofibers were grown on the graphene-Ni foam by a simple hydrothermal method. During the hydrothermal process, S ions released from thioacetamide react with Ni foam to produce Ni<sub>3</sub>S<sub>2</sub> particles or Ni<sub>3</sub>S<sub>2</sub> nanofibers [40,41], and then Ni<sub>3</sub>S<sub>2</sub> nanofibers act as a skeleton to guide the formation of ammonium intercalated MoS<sub>2</sub> nanosheet [42]. As shown in Fig. 1a, the well-defined MoS<sub>2</sub> nanosheet decorated Ni<sub>3</sub>S<sub>2</sub> nanofibers are preserved and the graphene wrapped Ni

foam electrode is uniformly covered by nanofibers with a diameter of 100 nm. The high magnification view of SEM reveals that the surface of Ni<sub>3</sub>S<sub>2</sub> nanofibers are covered by wrinkled ultrathin MoS<sub>2</sub> nanosheets.

It has been reported previously that S edge sites can effectively absorb H with a small free energy, which is advantageous for enhancing the HER activity [18–21]. Therefore, it is believed that wrinkled MoS<sub>2</sub> nanosheets with abundant active S sites should give an outstanding HER performances. The nanosheets are in tight contact with Ni<sub>3</sub>S<sub>2</sub> nanofibers, which is essential for long-term stability for hydrogen evolution reaction. To better elucidate the core-shell structure of A-MoS<sub>2</sub>/Ni<sub>3</sub>S<sub>2</sub> nanofibers, TEM images were carried out with a single nanofiber (Fig. 2a). MoS<sub>2</sub> nanosheets are grown tightly on Ni<sub>3</sub>S<sub>2</sub> nanofibers after the hydrothermal process, which is even strong enough against ultrasonication. The diameter of the nanofibers is about 100 nm. HRTEM image reveals lattice fringes of the Ni<sub>3</sub>S<sub>2</sub> core with characteristic planes of (101) and (110) and layered structure of the MoS<sub>2</sub> shell (Fig. 2b). The EDS mapping of a nanofiber displays the elemental Mo, Ni, S and N, revealing that all the elements are uniformly distributed in the A-MoS<sub>2</sub>/Ni<sub>3</sub>S<sub>2</sub> nanofibers (Fig. 2c and d). The detection of N signal by EDS also proves the successful ammonium intercalation in MoS<sub>2</sub> nanosheets.

The XRD patterns (Fig. 1c) were performed on MNG-120 sample (see Experimental Section for the assignment of sample names) to investigate crystallographic structure information. The two strong peaks at 2θ = 44.7 and 52.1 arise from the Ni foam substrate. The diffraction peaks at 2θ = 21.5, 30.9, 37.6, 49.5 and 55 correspond to the (101), (110), (003), (113), (211), (122) and (300) planes of Ni<sub>3</sub>S<sub>2</sub> (JCPDS no. 44-1418). Three characteristic diffraction peaks at 2θ = 32.0, 39.8 and 56.6 are assigned to (100), (103) and (110) planes of hexagonal MoS<sub>2</sub> (JCPDS No. 37-1492), a new peak arise at 2θ = 9.3° is assigned to the expanded (002) d spacing. The basal spacing increase is calculated to be 3.4 Å by the Scherrer's equation and matches with the size of NH<sub>3</sub> and NH<sub>4</sub><sup>+</sup> ion whose diameter is ~3.5 Å [43,44]. Further insight into the nanostructure of A-MoS<sub>2</sub>/Ni<sub>3</sub>S<sub>2</sub> is obtained by Raman spectrum (Fig. 1d). The E<sub>12g</sub> and A<sub>1g</sub> vibrational modes are located at 378 and 403 cm<sup>-1</sup>. Three additional peaks emerging at 192, 215 and 340 cm<sup>-1</sup> indicate the presence of 1T phase MoS<sub>2</sub> [36,38]. The strong peak at 284 cm<sup>-1</sup> is related with the Raman modes of Ni<sub>3</sub>S<sub>2</sub> [45].

X-ray photoelectron spectroscopy (XPS) was employed to characterize the chemical nature and bonding state of A-MoS<sub>2</sub>/Ni<sub>3</sub>S<sub>2</sub>. Fig. 3 displays the detailed XPS scans for the Mo, Ni, S and N binding energies. All spectra were calibrated by a carbon 1s peak located at 284.50 eV. Besides the peaks at 229.3 and 232.4 eV assigned to Mo 3d<sub>5/2</sub> and Mo 3d<sub>3/2</sub> for the 2H-MoS<sub>2</sub>, the 1T-MoS<sub>2</sub> peaks at 228.4 and 231.5 eV were obtained after the deconvolution of the Mo 3d spectrum, with a separation of binding energy at ~0.9 eV [33,34,38]. The S 2p doublet peaks exhibit broader peaks which could result from the bridging S<sub>2</sub><sup>2-</sup> or apical S<sup>2-</sup> atoms [46]. Fig. 3b shows two main peaks located at 874.3 and 856.1 eV which can be attributed to Ni 2p 1/2 and Ni 2p 3/2, respectively. Two satellite peaks with binding energies of 860.9 and 879.7 eV corresponding to metallic Ni [47,48]. The existence of intercalated NH<sub>4</sub><sup>+</sup> in the MNG-120 sample is demonstrated by the N1s spectrum of located at 398.3 eV [49,50].

The morphology of the MNG cathode, which is crucial to its HER performance can be easily controlled by the amount of thioacetamide (TAA) in the hydrothermal process. Fig. 4b–e shows the SEM images of the obtained A-MoS<sub>2</sub>/Ni<sub>3</sub>S<sub>2</sub> nanofibers prepared with different concentration of the TAA. For the sample MNG-30 with a low content of TAA (30 mg), only Ni<sub>3</sub>S<sub>2</sub> nanoparticles can be observed on the graphene-Ni foam, and no MoS<sub>2</sub> shell was formed. With increasing the content of TAA to 60 and 90 mg, Ni<sub>3</sub>S<sub>2</sub>

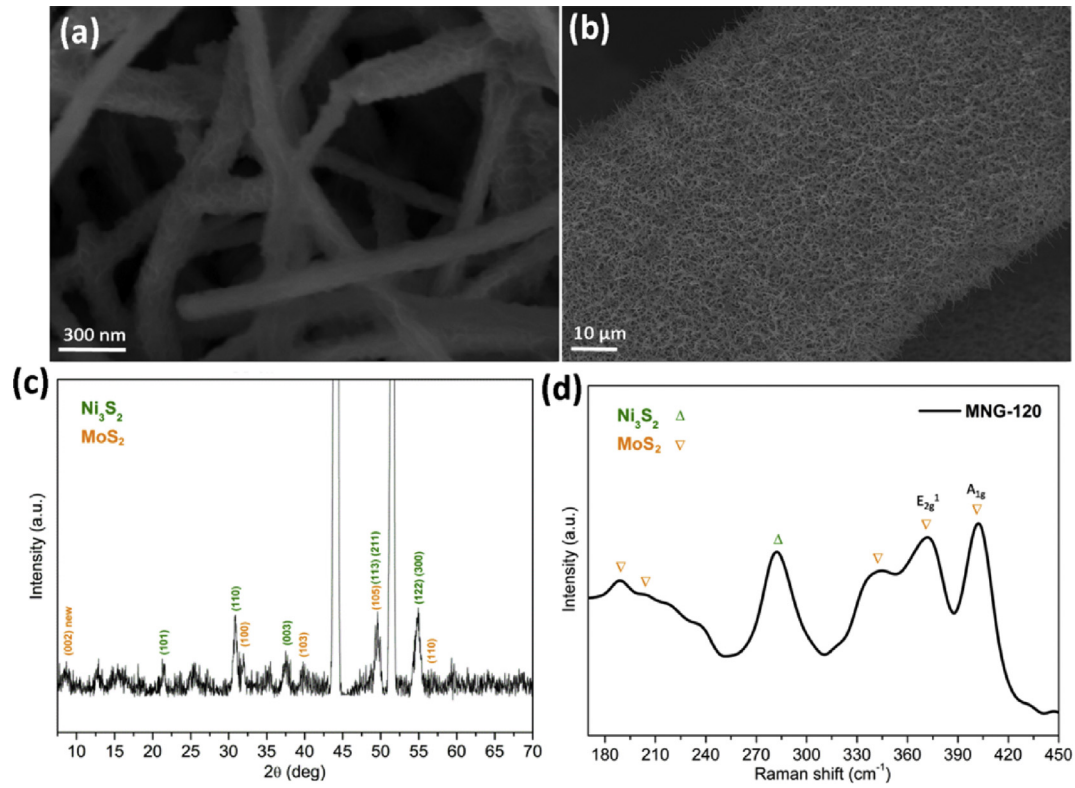


**Fig. 1.** (a) and (b) SEM micrographs of the A-MoS<sub>2</sub>/Ni<sub>3</sub>S<sub>2</sub> nanofiber structures with different magnifications. (c) XRD pattern, (d) Raman spectra of A-MoS<sub>2</sub>/Ni<sub>3</sub>S<sub>2</sub>/GN.

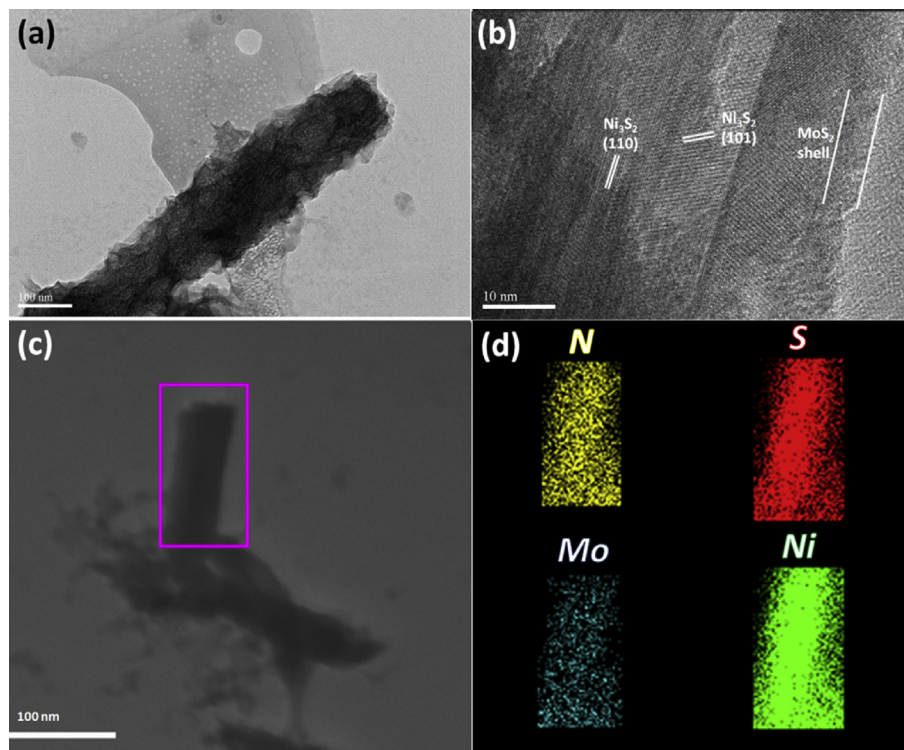


**Fig. 2.** (a) and (b) TEM micrographs of A-MoS<sub>2</sub>/Ni<sub>3</sub>S<sub>2</sub> nanofiber. (c) and (d) EDS mapping images of an individual nanofiber, indicating the ammonium intercalated MoS<sub>2</sub> nanosheet decorated Ni<sub>3</sub>S<sub>2</sub> nanofiber hierarchical structure.

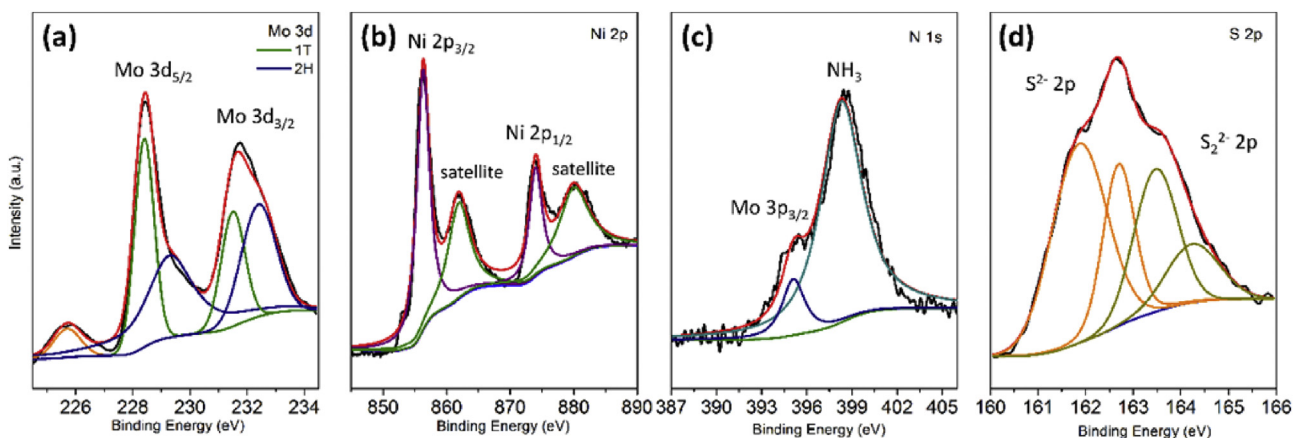


Fig. 3. XPS spectra showing Mo 3d (a), Ni 2p (b), N 1s (c) and S 2p (d) peaks core level peak regions.

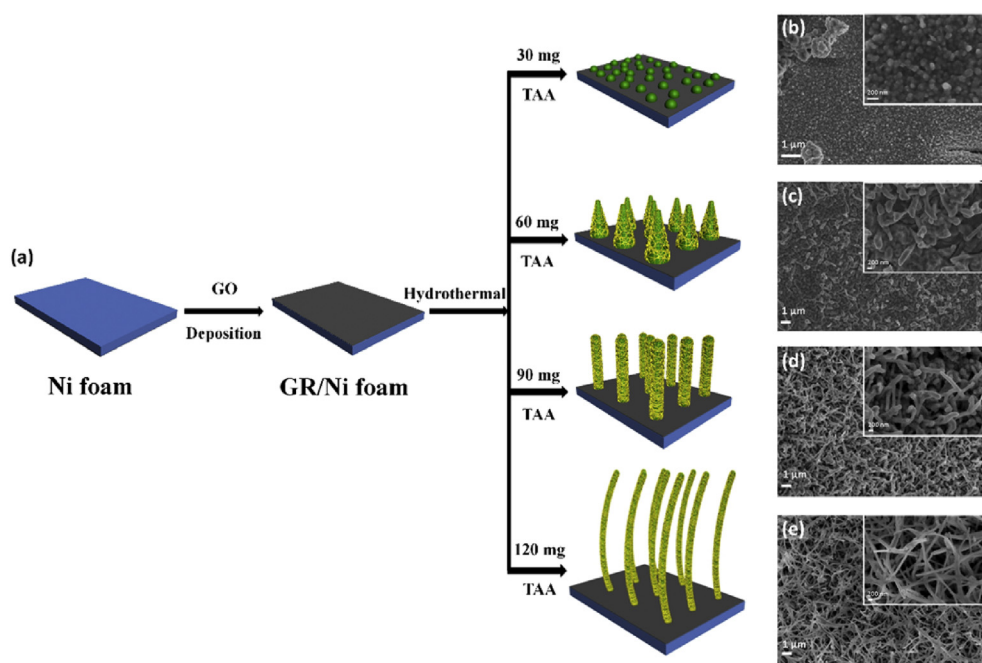
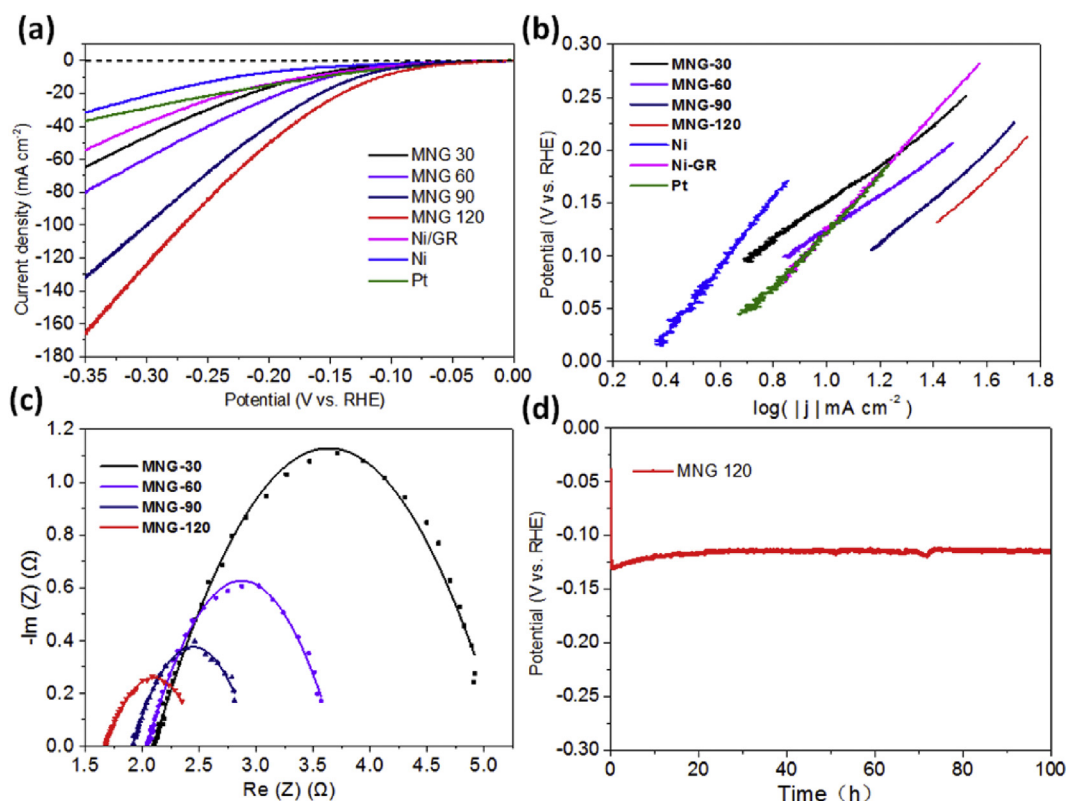


Fig. 4. (a) Schematic illustration of the obtained MoS<sub>2</sub> decorated Ni<sub>3</sub>S<sub>2</sub> nanostructures obtained from different content of thioacetamide. SEM images of MoS<sub>2</sub> decorated Ni<sub>3</sub>S<sub>2</sub> nanostructures obtained from different content of thioacetamide: (b) 30 mg, (c) 60 mg, (d) 90 mg and (e) 120 mg.

nanoparticles gradually evolve to nanopyramids and nanorods, and the coverage of MoS<sub>2</sub> nanosheets increases. By increasing the content of TAA to 120 mg, Ni<sub>3</sub>S<sub>2</sub> nanorods become thinner and longer. MoS<sub>2</sub> ultrathin nanosheets uniformly cover on the Ni<sub>3</sub>S<sub>2</sub> nanofibers. Graphene-Ni foam is fully coated by A-MoS<sub>2</sub>/Ni<sub>3</sub>S<sub>2</sub> nanofibers. The corresponding schematic illustration for the formation of the above samples is proposed in Fig. 4a. Based on the observations described above, the content of sulfur source plays a key role in the formation of the core/shell nanostructures. During the hydrothermal process, the S ions released from TAA first react with the Ni foam to form small Ni<sub>3</sub>S<sub>2</sub> particles on the surface of graphene. As the content increases, these nanoparticles grow into nanorods and then nanofibers, which act as the template to guide the self-assembly of MoS<sub>2</sub> nanosheets.

The HER performance of the MNG samples with different morphologies were measured in 1 M KOH solution using a typical three-electrode setup at a scan rate of 0.5 mV/s. The polarization curves in Fig. 5a shows that all the A-MoS<sub>2</sub>/Ni<sub>3</sub>S<sub>2</sub> composites

exhibit a relatively higher HER activity to the Pt and Ni foam. Notably, MNG-120 exhibits a low overpotential of 109 mV to achieve a cathodic current density of 10 mA cm<sup>-2</sup>. The overpotential decreases in the following order: Ni > Pt gauze (1 cm<sup>-2</sup>) > Ni-GR > MNG-30 > Ni<sub>3</sub>S<sub>2</sub> fibers > MNG-60 > MNG-90 > MNG-120. The overpotential of MNG-120 sample is lower than those of previously reported nanostructured electrocatalysts consists of earth-abundant elements (Table S1). Correcting the polarization data of MNG-120 for iR correction (Fig. S3) revealed more impressive performance, as cathodic current densities of 10 and 100 mA cm<sup>-2</sup> were achieved at low overpotentials of -103 and -166 mV vs RHE, respectively. To investigate the intrinsic HER kinetics of the catalysts, Tafel slopes were obtained from the Tafel equation. As shown in Fig. 5b, the Tafel slope of MNG-120 (120 mV dec<sup>-1</sup>) is smaller than Pt, Ni foam and GN. Such a Tafel slope value in the range of 40–120 mV dec<sup>-1</sup>, indicating that the hydrogen generation would proceed via Volmer-Heyrovsky mechanism on the surface of A-MoS<sub>2</sub>/Ni<sub>3</sub>S<sub>2</sub> composites [30,51,52].



**Fig. 5.** (a) Polarization curves and (b) corresponding Tafel plots of MNG, Ni foam, Ni-GR and Pt. The curves were recorded in 1 M KOH solution at a scan rate of 0.5 mV/s. (c) EIS spectra of MNG with  $-0.2$  V vs. RHE in 1 M KOH electrolyte. (d) Chronopotentiometry curves of the MNG-120 at a constant current density of  $10 \text{ mA cm}^{-2}$ .

To understand the HER interface reactions kinetics mechanism, electrochemical impedance spectroscopy (EIS) measurements were obtained. Fig. 5c shows the Nyquist plots of the MNG samples. The series resistances ( $R_s$ ) are found to be  $1.7\text{--}2.1 \Omega$  which comes from wiring contact and the electrolyte. The semicircular diameter in the high-frequency region of the MNG-120 composites is much less than that of MNG-30, MNG-60 and MNG-90, indicating enhanced interfacial charge transfer kinetics. The lower  $R_{ct}$  of the MNG-120 can be attributed to the higher HER catalytic activity of A-MoS<sub>2</sub> [53]. To probe the stability of A-MoS<sub>2</sub>/Ni<sub>3</sub>S<sub>2</sub> nanofibers catalysts during HER process, a long-term durability test was conducted at constant current of  $10 \text{ mA cm}^{-2}$ . Fig. 5d displays the chronopotentiometry, showing no obvious decay in the potential after 100 h, revealing the excellent stability to withstand a long-term HER process in strong alkaline media. Small H<sub>2</sub> bubbles can be timely released on the superaerophobic surfaces, which ensures an intimate solid-liquid interface contact [54]. The XPS characterization further verifies that the intercalated ammonium is well preserved after long durability test (Fig. S4).

The double layer capacitances ( $C_{dl}$ ) were measured by plotting the  $\Delta j$  ( $J_{aE} - J_c$ ) at 0.15 V vs. RHE against the scan rate (Fig. S5) to estimate the electrochemical surface area (ECSA) at the solid-liquid interface. The  $C_{dl}$  were calculated to be 1610 mF for MNG-120, significantly larger than MNG-30 (70 mF), MNG-60 (125 mF) and MNG-90 (881 mF). This result reveals that MNG-120 has the highest effective electrochemical active area among all the A-MoS<sub>2</sub>/Ni<sub>3</sub>S<sub>2</sub> catalysts. In addition, to estimate the mass numbers of active sites of the MNG samples, a simple cyclic voltammetry measurements in the region of  $-0.2$  to  $0.6$  V vs. RHE were carried out in 1 M KOH solution (Fig. S6) [55]. The enclosed area of MNG-120 is obviously larger than that of the other MNG samples.

To calculate and compare the difference in the Gibbs free energy for hydrogen adsorption on the (002) plan surfaces of the 2H and 1T phase MoS<sub>2</sub> with first principles calculations, we consider optimized structures of 2H and 1T MoS<sub>2</sub> model, both of which has an expansion in its c direction due to intercalation of ammonium ions (Fig. 6a and c). For the 2H model, we construct a modified 48 atoms (16 Molybdenum atoms and 32 Sulfur atoms) unit cell, in which the interlayer distance enlarges from the pristine 6.15 Å to 9.5 Å due to two ammonium ions inserted in each two layers (Fig. 6a). While for the 1T phase model, we consider a different stacking structure, in which the unit cell has three layers instead of two layers as in the pristine 2H phase. We also construct a modified 72 atoms (24 Molybdenum atoms and 48 Sulfur atoms) unit cell with an interlayer distance of 9.5 Å due to two ammonium ions inserted in each two layers (Fig. 6c), which is consistent with our experimental data. After the two models are fully relaxed, we calculate the Gibbs free energies for hydrogen adsorption on the (002) plan surfaces of the two relaxed systems. One hydrogen atom is adsorbed on sulfur atom for each layer slab (Fig. 6b and d). The DFT calculated binding energies contain no contributions from zero-point energies and entropy, and these contributions were added separately in order to obtain the Gibbs free energies.

The stability of hydrogen was described by the differential hydrogen chemisorption energy  $\Delta G$ , which is calculated as follows, for the ammonium ions intercalation MoS<sub>2</sub> systems:

$$\Delta G_H = E(\text{NH}_4^+ - \text{MoS}_2 + n\text{H}) - E(\text{NH}_4^+ - \text{MoS}_2 + (n-1)\text{H}) - n/2E(\text{H}_2)$$

where  $E(\text{NH}_4^+ - \text{MoS}_2 + n\text{H})$  are the DFT calculated total energy for the two kinds of ammonium ions intercalated MoS<sub>2</sub> systems, with  $n$

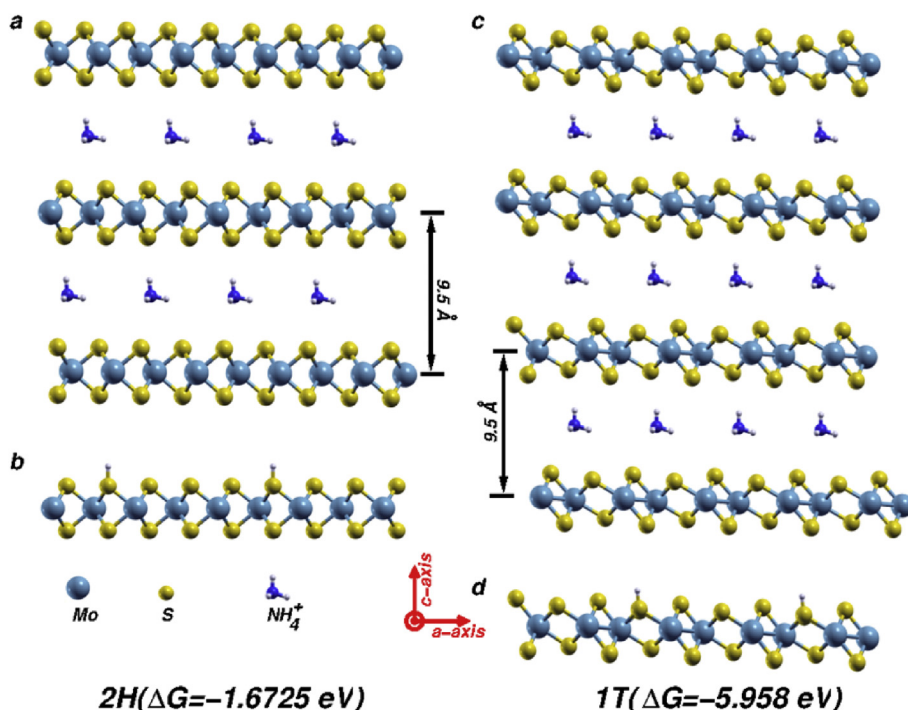


**Fig. 6.** (a, c) The  $2 \times 1 \times 1$  supercell optimized structure of ammonium ions inserted 2H and 1T  $\text{MoS}_2$  along the c-axis. (b, d) Hydrogen atoms adsorbed on each layer slab of  $2 \times 1 \times 1$  supercell optimized structure of ammonium ions inserted 2H and 1T  $\text{MoS}_2$ .

hydrogen atoms adsorbed on each layer slab, and  $E(\text{NH}_4^+ - \text{MoS}_2 + (n-1)\text{H})$  is the calculated total energy for  $(n-1)$  hydrogen atoms adsorbed on each layer slab, and  $E(\text{H}_2)$  is the calculated energy for a hydrogen molecule in the gas phase. The ammonium intercalated A- $\text{MoS}_2$  possesses a much lower differential binding free energy of  $-5.958 \text{ eV}$  than 2H phase  $\text{MoS}_2$  of  $-1.6725 \text{ eV}$ . Thus, the (002) surface of A- $\text{MoS}_2$  exhibits superior binding activity toward H-chemisorption. A higher H coverage can be achieved at lower overpotential for the ammonium intercalated A- $\text{MoS}_2$  catalyst, providing more effective sites for HER catalysis [25,56,57].

Encouraged by the outstanding HER performance in alkaline media, a two-electrode electrolyzer using A- $\text{MoS}_2/\text{Ni}_2\text{S}_3$  catalysts as the cathode and nickel iron layered double hydroxides (NiFe-LDH) as the anode was assembled for overall water splitting in 1 M KOH

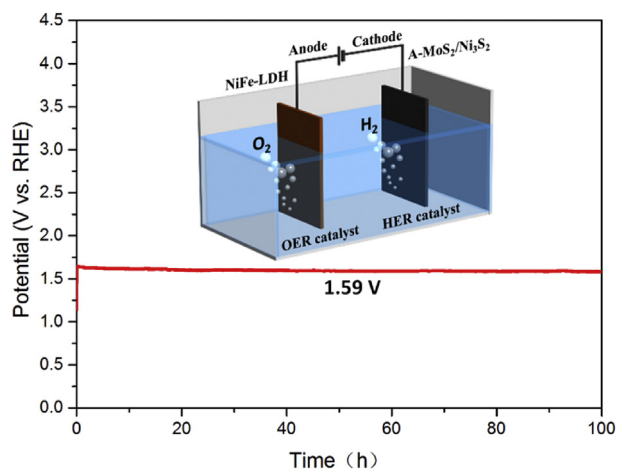


**Fig. 7.** Chronopotentiometry curves of the two-electrode electrolyzer (NiFe-LDH||A- $\text{MoS}_2/\text{Ni}_2\text{S}_3$ ) at a constant current density of  $10 \text{ mA cm}^{-2}$  in 1 M KOH electrolyte. Inset: schematic of the electrolyzer.

(Fig. S7). The assembled water-splitting cell drive a water splitting current density of  $10 \text{ mA m}^{-2}$  at an applied voltage of just 1.59 V (Fig. 7), which is comparable to that of reported electrocatalysts, as well as the reported the state-of-the-art bi-functional electrocatalysts (Table S2). After 100 h of electrolysis reaction, the NiFe-LDH||A- $\text{MoS}_2/\text{Ni}_2\text{S}_3$  still exhibited high activity without a noticeable decay for overall water splitting, indicating its high stability over long-term operation as promising practical applications.

### 3. Conclusion

In summary, ammonium intercalated  $\text{MoS}_2/\text{Ni}_3\text{S}_2$  core-shell nanofiber structure on graphene-Ni foam electrocatalyst with large surface area were fabricated by a convenient method. The combined DFT and experimental results show that the ammonium ions intercalate into  $\text{MoS}_2$  nanosheets can facilitate the formation of 1T phase and efficiently lower the Gibbs free energy for protons chemisorption. Benefiting from the large surface area, high conductivity, as well as more effective sites, this hierarchical electrocatalyst exhibits extremely low overpotential of 109 mV at  $10 \text{ mA cm}^{-2}$  and long-term durability in alkali medium for HER catalysis. Moreover, we demonstrated an efficient and stable overall water splitting cell consisted of NiFe-LDH||A- $\text{MoS}_2/\text{Ni}_2\text{S}_3$ , which exhibited a current density of  $10 \text{ mA cm}^{-2}$  at a cell voltage of as low as 1.59 V with remarkable stability. Considering their excellent electrolytic activity for HER, this facile and scale-up approach can be readily extended to synthesize other self-supported transition metal sulfide for renewable energy system.

### 4. Experimental section

#### 4.1. Synthesis of graphene-Ni foam

Graphene oxide was synthesized from natural graphite by a modified Hummer's method. The graphene nanosheets were

deposited on the nickel foam through interfacial reduction method to form three-dimensional graphene wrapped Ni (GN) architecture. In detail, a piece of Ni foam (1.6 mm thick) was washed with acetic acid and deionized water. Then the Ni foam was immersed into a GO suspension at 80 °C for 6 h. During this process, black graphene films can spontaneously grow on the surface of Ni networks. After cooling to room temperature, the GN was washed with deionized water for several times and dried in an oven at 60 °C for 12 h.

#### 4.2. Synthesis of A-MoS<sub>2</sub>/Ni<sub>3</sub>S<sub>2</sub>/graphene-Ni foam hybrid structure

Ammonium intercalated MoS<sub>2</sub> nanosheet decorated Ni<sub>3</sub>S<sub>2</sub> nanofibers were prepared using a facile hydrothermal method. In detail, 0.09 g sodium molybdate (Na<sub>2</sub>MoO<sub>4</sub>·2H<sub>2</sub>O), 0.12 g thioacetamide (C<sub>2</sub>H<sub>5</sub>NS) and 0.3 g urea were dissolved in a 100 mL Teflon-line stainless steel autoclave under vigorous stirring. A piece of graphene-nickel foam (8 cm<sup>-2</sup>) was vertically immersed into the reaction solution. The autoclave was then sealed and the hydrothermal reaction was conducted at 180 °C for 12 h. The samples were prepared with 30, 60, 90 and 120 mg of thioacetamide (C<sub>2</sub>H<sub>5</sub>NS), which were labeled as MNG-30, MNG-60, MNG-90 and MNG-120, respectively. For comparison, Ni<sub>3</sub>S<sub>2</sub> nanofibers on graphene-Ni foam were synthesized under the same conditions without the addition of sodium molybdate.

#### 4.3. Synthesis of NiFe-LDH on Ni foam

Briefly, 0.3 g nickel nitrate (Ni(NO<sub>3</sub>)<sub>2</sub>), 0.4 g ferric nitrate (Fe(NO<sub>3</sub>)<sub>3</sub>), 0.6 g urea and 80 mL deionized water were placed into a 100 mL Teflon-line stainless steel autoclave. A piece of graphene-nickel foam (8 cm<sup>-2</sup>) was vertically immersed into the reaction solution. The autoclave was then sealed and the hydrothermal reaction was conducted at 120 °C for 12 h. After cooling down to room temperature, the samples was rinsed with deionized water.

#### 4.4. Materials characterizations

The surface morphology was analyzed by SEM (FEI Sirion 200) and TEM (JEOL 2100F). The crystallinity structures were characterized with X-ray diffraction (XRD) by a Japan Rigaku Ultima IV equipped with Cu K $\alpha$  radiation. The chemical states of surface composition were determined by XPS (AXIS ULTRA DLD, Kratos, Japan). Raman spectroscopy was recorded on Renishaw in Via-reflex system equipped with an excitation 532 nm wavelength laser at room temperature.

#### 4.5. Electrochemical measurements

Electrochemical measurements were performed in a three-electrode system on a PARSTAT 4000 workstation. Linear sweep voltammetry with scan rate of 0.5 mV/s was conducted in 1 M KOH, using the prepared samples as the working electrodes, a Pt gauze as the counter electrode, and Ag/AgCl as a reference electrode. The electrochemical impedance spectroscopy (EIS) measurements were performed in 1 M KOH solution with the frequencies range from 10 KHz to 0.1 Hz with an AC voltage of 5 mV. All the potentials reported in our manuscript were referenced to a reversible hydrogen electrode (RHE) by the Nernst equation  $E_{RHE} = E_{Ag/AgCl} + 0.059 \text{ pH} + 0.197$ .

The overall water splitting was carried in a two-electrode system in 1.0 M KOH solution, in which the A-MoS<sub>2</sub>/Ni<sub>3</sub>S<sub>2</sub>/graphene-Ni foam was directly used as the cathode and the NiFe-LDH on Ni foam was used as anode at a constant current density of 10 mA cm<sup>-2</sup>.

#### 4.6. First-principles calculations methods

To explain our experimental findings that suggest the effect of ammonium intercalated MoS<sub>2</sub> structure on the chemisorption of hydrogen, first-principles calculations based on the density functional theory were performed using the Vienna Ab initio Simulation Package (VASP) code, adopting the projector augmented wave (PAW) potential [58], the generalized-gradient-approximation (GGA) with the exchange-correlation functional of GGA-PBE as parameterized by Perdew, Burke and Ernzerhof [59] and a plane-wave basis set. A 500 eV energy cutoff and 2 × 4 × 2, 2 × 4 × 1 Monkhorst-Pack k-point grids [60] were used for the ammonium intercalated the structures of 2H phase and 1T phase MoS<sub>2</sub> given in Fig. 6a and c. When performing geometric optimization, the lattice constant and atomic positions are fully relaxed, with the energy convergence of about 1 meV per atom and the residual stresses and force in the fully relaxed structures being less than 0.1 GPa and 0.001 eV/Å.

#### Data availability statement

The raw/processed data required to reproduce these findings cannot be shared at this time due to technical or time limitations.

#### Acknowledgment

This work was supported by National 863 Program 2011AA050518, the Natural Science Foundation of China (Grant nos. 11174197, 11574203, 61234005, and 21872019). Y. Li acknowledges financial support of National 1000 Talents Program of China.

#### Appendix A. Supplementary data

Supplementary data to this article can be found online at <https://doi.org/10.1016/j.mtener.2018.09.004>.

#### References

- [1] T.R. Cook, D.K. Dogutan, S.Y. Reece, Y. Surendranath, T.S. Teets, D.G. Nocera, *Chem. Rev.* 110 (2010) 6474.
- [2] N.S. Lewis, D.G. Nocera, *Proc. Natl. Acad. Sci.* 103 (2006) 15729.
- [3] T.E. Mallouk, *Nat. Chem.* 5 (2013) 362.
- [4] K. Zeng, D. Zhang, *Prog. Energy Combust. Sci.* 36 (2010) 307.
- [5] C.G. Morales-Guio, L.-A. Stern, X. Hu, *Chem. Soc. Rev.* 43 (2014) 6555.
- [6] X. Zou, Y. Zhang, *Chem. Soc. Rev.* 44 (2015) 5148.
- [7] D.V. Esposito, S.T. Hunt, A.L. Stottlemeyer, K.D. Dobson, B.E. McCandless, R.W. Birkmire, J.G. Chen, *Angew. Chem. Int. Ed.* 49 (2010) 9859.
- [8] J. Sun, H. Yin, P. Liu, Y. Wang, X. Yao, Z. Tang, H. Zhao, *Chem. Sci.* 7 (2016) 5640.
- [9] H. Yin, Z. Tang, *Chem. Soc. Rev.* 45 (2016) 4873.
- [10] S. Zhao, Y. Wang, J. Dong, C.-T. He, H. Yin, P. An, K. Zhao, X. Zhang, C. Gao, L. Zhang, J. Lv, J. Wang, J. Zhang, A.M. Khattak, N.A. Khan, Z. Wei, J. Zhang, S. Liu, H. Zhao, Z. Tang, *Nat. Energy* 1 (2016) 16184.
- [11] D.-Y. Wang, M. Gong, H.-L. Chou, C.-J. Pan, H.-A. Chen, Y. Wu, M.-C. Lin, M. Guan, J. Yang, C.-W. Chen, Y.-L. Wang, B.-J. Hwang, C.-C. Chen, H. Dai, *J. Am. Chem. Soc.* 137 (2015) 1587.
- [12] G. Huang, H. Liu, S. Wang, X. Yang, B. Liu, H. Chen, M. Xu, *J. Mater. Chem. A* 3 (2015) 24128.
- [13] J. Zhang, S. Liu, H. Liang, R. Dong, X. Feng, *Adv. Mater.* 27 (2015) 7426.
- [14] A.B. Laursen, S. Kegnaes, S. Dahl, I. Chorkendorff, *Energy Environ. Sci.* 5 (2012) 5577.
- [15] Y. Yan, B. Xia, Z. Xu, X. Wang, *ACS Catal.* 4 (2014) 1693.
- [16] D. Merki, X. Hu, *Energy Environ. Sci.* 4 (2011) 3878.
- [17] G. Zhang, H. Liu, J. Qu, J. Li, *Energy Environ. Sci.* 9 (2016) 1190.
- [18] T.F. Jaramillo, K.P. Jørgensen, J. Bonde, J.H. Nielsen, S. Horch, I. Chorkendorff, *Science* 317 (2007) 100.
- [19] H.I. Karunadasa, E. Montalvo, Y. Sun, M. Majda, J.R. Long, *C. J. Chem. Science* 335 (2012) 698.
- [20] B. Hinnemann, P.G. Moses, J. Bonde, K.P. Jørgensen, J.H. Nielsen, S. Horch, I. Chorkendorff, J.K. Nørskov, *J. Am. Chem. Soc.* 127 (2005) 5308.
- [21] Y. Huang, R.J. Nielsen, W.A. Goddard, M.P. Soriaga, *J. Am. Chem. Soc.* 137 (2015) 6692.
- [22] H. Yu, X. Yu, Y. Chen, S. Zhang, P. Gao, C. Li, *Nanoscale* 7 (2015) 8731.
- [23] J. Kibsgaard, Z. Chen, B.N. Reinecke, T.F. Jaramillo, *Nat. Mater.* 11 (2012) 963.

- [24] J. Xie, H. Zhang, S. Li, R. Wang, X. Sun, M. Zhou, J. Zhou, X.W. Lou, Y. Xie, *Adv. Mater.* 25 (2013) 5807.
- [25] J. Xie, J. Zhang, S. Li, F. Grote, X. Zhang, H. Zhang, R. Wang, Y. Lei, B. Pan, Y. Xie, *J. Am. Chem. Soc.* 135 (2013) 17881.
- [26] J. Deng, H. Li, J. Xiao, Y. Tu, D. Deng, H. Yang, H. Tian, J. Li, P. Ren, X. Bao, *Energy Environ. Sci.* 8 (2015) 1594.
- [27] D. McAteer, Z. Gholamvand, N. McEvoy, A. Harvey, E. O'Malley, G.S. Duesberg, J.N. Coleman, *ACS Nano* 10 (2016) 672.
- [28] Y. Yan, X. Ge, Z. Liu, J.-Y. Wang, J.-M. Lee, X. Wang, *Nanoscale* 5 (2013) 7768.
- [29] D.J. Li, U.N. Maiti, J. Lim, D.S. Choi, W.J. Lee, Y. Oh, G.Y. Lee, S.O. Kim, *Nano Lett.* 14 (2014) 1228.
- [30] Y. Li, H. Wang, L. Xie, Y. Liang, G. Hong, H. Dai, *J. Am. Chem. Soc.* 133 (2011) 7296.
- [31] T.-N. Ye, L.-B. Lv, M. Xu, B. Zhang, K.-X. Wang, J. Su, X.-H. Li, J.-S. Chen, *Nano Energy* 15 (2015) 335.
- [32] Y. Yin, J. Han, Y. Zhang, X. Zhang, P. Xu, Q. Yuan, L. Samad, X. Wang, Y. Wang, Z. Zhang, P. Zhang, X. Cao, B. Song, S. Jin, *J. Am. Chem. Soc.* 138 (2016) 7965.
- [33] H. Wang, Z. Lu, S. Xu, D. Kong, J.J. Cha, G. Zheng, P.-C. Hsu, K. Yan, D. Bradshaw, F.B. Prinz, Y. Cui, *Proc. Natl. Acad. Sci.* 110 (2013) 19701.
- [34] H. Wang, Z. Lu, D. Kong, J. Sun, T.M. Hymel, Y. Cui, *ACS Nano* 8 (2014) 4940.
- [35] H. Tang, J. Wang, H. Yin, H. Zhao, D. Wang, Z. Tang, *Adv. Mater.* 27 (2015) 1117.
- [36] M.A. Lukowski, A.S. Daniel, F. Meng, A. Forticaux, L. Li, S. Jin, *J. Am. Chem. Soc.* 135 (2013) 10274.
- [37] D. Voiry, M. Salehi, R. Silva, T. Fujita, M. Chen, T. Asefa, V.B. Shenoy, G. Eda, M. Chhowalla, *Nano Lett.* 13 (2013) 6222.
- [38] G. Eda, H. Yamaguchi, D. Voiry, T. Fujita, M. Chen, M. Chhowalla, *Nano Lett.* 11 (2011) 5111.
- [39] F.Z. Wang, M.J. Zheng, B. Zhang, C.Q. Zhu, Q. Li, L. Ma, W.Z. Shen, *Sci. Rep.* 6 (2016) 31092.
- [40] W. Zhou, X. Cao, Z. Zeng, W. Shi, Y. Zhu, Q. Yan, H. Liu, J. Wang, H. Zhang, *Energy Environ. Sci.* 6 (2013) 2216.
- [41] J. Wang, J. Liu, H. Yang, D. Chao, J. Yan, S.V. Savilov, J. Lin, Z.X. Shen, *Nano Energy* 20 (2016) 1.
- [42] J. Wang, D. Chao, J. Liu, L. Li, L. Lai, J. Lin, Z. Shen, *Nano Energy* 7 (2014) 151.
- [43] Z. Wu, C. Tang, P. Zhou, Z. Liu, Y. Xu, D. Wang, B. Fang, *J. Mater. Chem. A* 3 (2015) 13050.
- [44] F.R. Gamble, J.H. Osiecki, M. Cais, R. Pisharody, F.J. DiSalvo, T.H. Geballe, *Science* 174 (1971) 493.
- [45] W. Lai, Z. Chen, J. Zhu, L. Yang, J. Zheng, X. Yi, W. Fang, *Nanoscale* 8 (2016) 3823.
- [46] H. Vrubel, X. Hu, *ACS Catal.* 3 (2013) 2002.
- [47] C.E. Scott, M.J. Perez-Zurita, L.A. Carbognani, H. Molero, G. Vitale, H.J. Guzmán, P. Pereira-Almao, *Catal. Today* 250 (2015) 21.
- [48] C. Wang, D. Wang, Z. Wu, Z. Wang, C. Tang, P. Zhou, *Appl. Catal. A* 476 (2014) 61.
- [49] Q. Liu, X. Li, Q. He, A. Khalil, D. Liu, T. Xiang, X. Wu, L. Song, *Small* 11 (2015) 5556.
- [50] A. Anto Jeffery, C. Nethravathi, M. Rajamathi, *J. Phys. Chem. C* 118 (2014) 1386.
- [51] L. Liao, J. Zhu, X. Bian, L. Zhu, M.D. Scanlon, H.H. Girault, B. Liu, *Adv. Funct. Mater.* 23 (2013) 5326.
- [52] Y. Jiang, X. Li, S. Yu, L. Jia, X. Zhao, C. Wang, *Adv. Funct. Mater.* 25 (2015) 2693.
- [53] L. Zhang, H.B. Wu, Y. Yan, X. Wang, X.W. Lou, *Energy Environ. Sci.* 7 (2014) 3302.
- [54] Z. Lu, W. Zhu, X. Yu, H. Zhang, Y. Li, X. Sun, X. Wang, H. Wang, J. Wang, J. Luo, X. Lei, L. Jiang, *Adv. Mater.* 26 (2014) 2683.
- [55] Y. Yan, B. Xia, X. Ge, Z. Liu, J.-Y. Wang, X. Wang, *ACS Appl. Mater. Interfaces* 5 (2013) 12794.
- [56] J. Zhang, T. Wang, P. Liu, S. Liu, R. Dong, X. Zhuang, M. Chen, X. Feng, *Energy Environ. Sci.* 9 (2016) 2789.
- [57] J. Zhang, T. Wang, D. Pohl, B. Rellinghaus, R. Dong, S. Liu, X. Zhuang, X. Feng, *Angew. Chem. Int. Ed.* 55 (2016) 6702.
- [58] G. Kresse, D. Joubert, *Phys. Rev. B* 59 (1999) 1758.
- [59] J.P. Perdew, K. Burke, M. Ernzerhof, *Phys. Rev. Lett.* 77 (1996) 3865.
- [60] H.J. Monkhorst, J.D. Pack, *Phys. Rev. B* 13 (1976) 5188.